**SUPPLEMENTAL INFORMATION**

**SUPPLEMENTAL DATA**
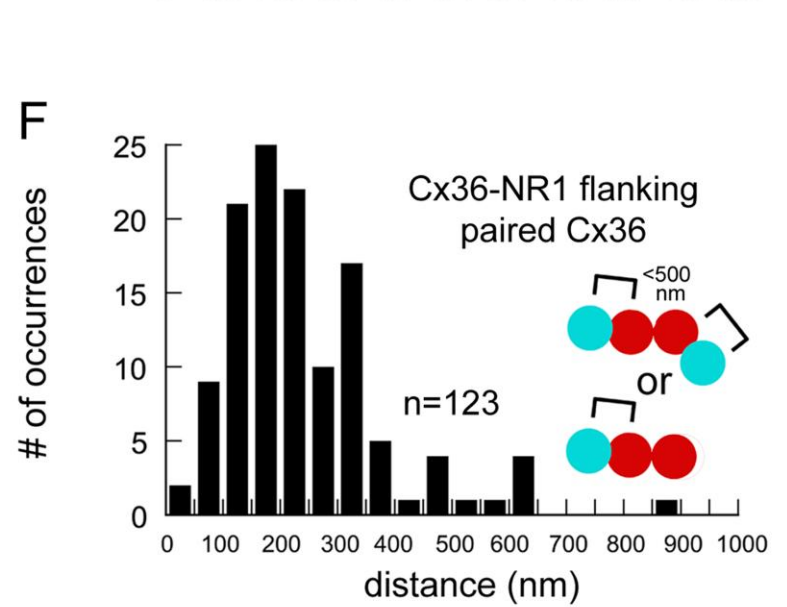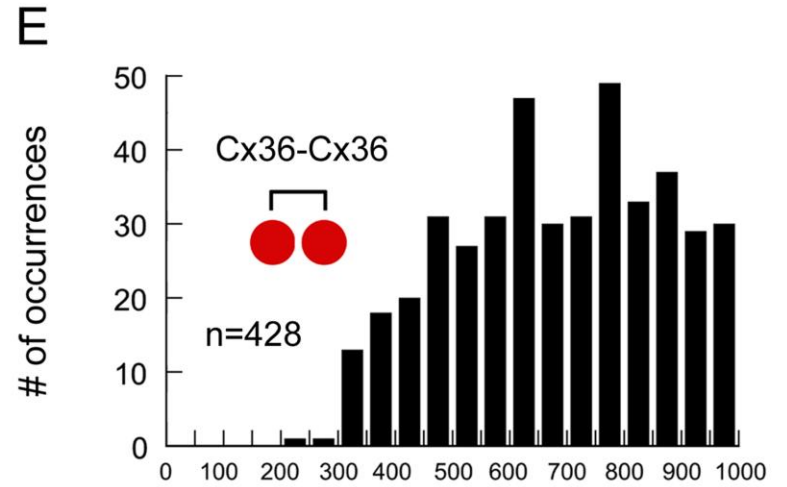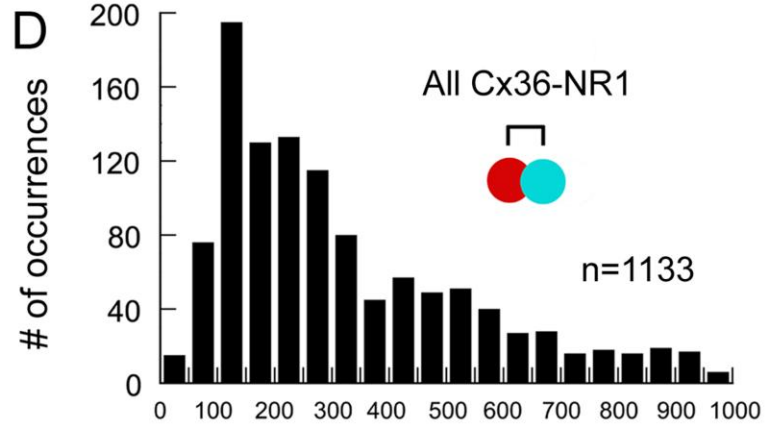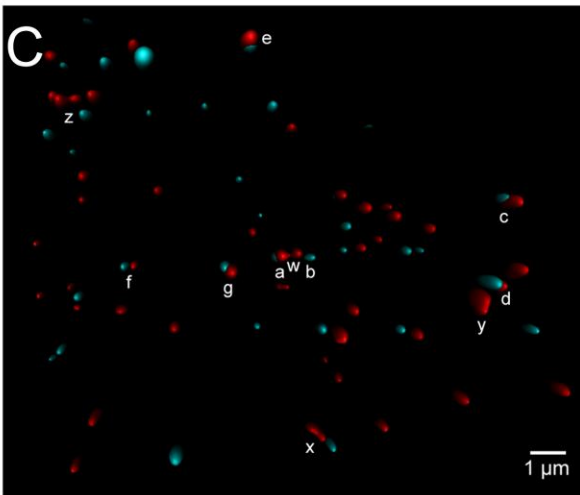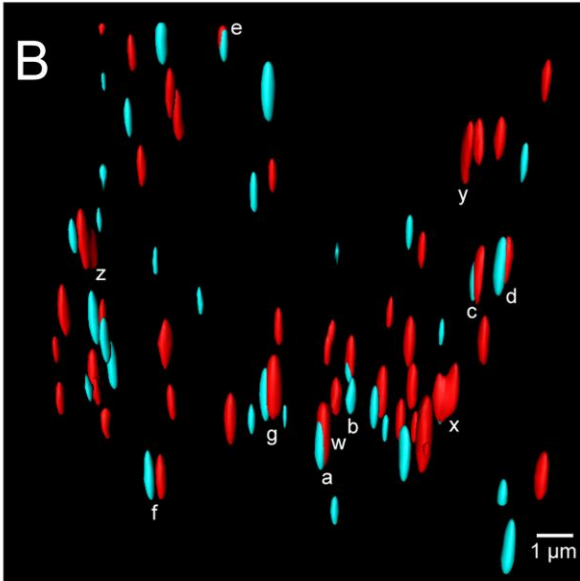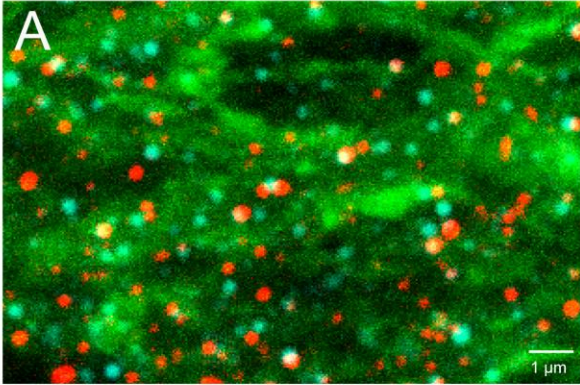
**Figure S1. Three-dimensional analysis of Cx36-NR1 spacing, related to Fig. 1.**

GFP was expressed IO neurons of Sprague-Dawley rats by stereotaxic injection of recombinant lentivirus ($10^8$ pfu/ml) containing the GFP coding sequence driven by the phosphoglycerate kinase promoter (Placantonakis et al., 2006). After 1 week survival, the rats were anesthetized by sodium pentobarbital (150 mg/kg, i.p.) and perfused with 10 ml heparinized saline (1000 units/ml), 50 ml 3.8% acrolein in 2% paraformaldehyde, 200 ml 2% paraformaldehyde in 0.1 M phosphate buffer (PB, pH 7.4). Brains were placed in 2% paraformaldehyde (30 min) and then 0.1 M PB. The brains were processed for double label immunohistochemistry of NR1 and Cx36 prior to multispectral confocal imaging. Sections (40 µm) were collected in 0.1 M PB, incubated in 1% sodium borohydride (30 min) to increase antigenicity, 0.5% bovine serum albumin to reduce non-specific binding, and then in anti-NR1 (1:100, 5 µg/ml, BD-Pharmingen) and anti-Cx36 (1:250, 2 µg/ml, Zymed) antisera. NR1 antibody was visualized following 2 h incubation in goat anti-mouse IgG conjugated to Alexa 647 (Molecular Probes, 1:800). Cx36 antibody was visualized using goat anti-rabbit IgG conjugated to Alexa 568 (1:800). A laser scanning confocal microscope (Zeiss LSM-710) and a 100x objective (Zeiss, alpha-plan Achromat 1.46 na) were used to obtain z-stacks (340 nm optical sections) of dendritic GFP (green) and Cx36 (red, Alexa 543) and NR1 (blue, Alexa 647) immunoreactivity (46 nm sampling, 8x averaging). Spectral bleed-through was prevented using alternating laser excitation and emission filtering. A 488 nm laser excited GFP (500-560 nm detected); a 543 nm laser excited Alexa 568 (600-652 nm detected); a 633 nm laser excited Alexa 647 (650-720 nm detected). A representative projection through a z-stack (14.3 x 10.7 x 13.6 µm) is shown in A and demonstrates the punctate appearance of Cx36 and NR1 immunoreactivity. Surface rendering of the three channels was performed with Imaris software

(Bitplane, South Windsor CT) using 9 nm interpolated smoothing and allowing rotation, translation, and clipping of the volumes through any axis. Surface-rendered volumes of the immunoreactivity in A are shown from a perspective perpendicular to the plane of laser excitation rotated by 20 degrees (B) and from above (C), slightly exploded along the x and y axes as the volume approaches the surface in order to demonstrate the relation between Cx36 and NR1 immunopuncta in 3 dimensions. The projections demonstrate that many Cx36 and NR1 puncta were spatially overlapping or closely-spaced (i.e. puncta labeled a through g) and that some pairs of neighboring Cx36 puncta were contiguous (i.e. w through z). Triple- or quadruple-assemblies of Cx36-NR1 puncta were observed (i.e. a-w-b) using this approach. Quantitation of the spatial proximity of Cx36 and NR1 puncta in the neuropil (D) for 1133 Cx36-NR1 pairs spaced closer than 1 µm shows a mode Cx36-NR1 distance of 125 nm with 10% of pairs spaced closer than 100 nm. Similar analysis of Cx36 pairs (E) shows a relatively flat distribution above the diffraction limit (190 µm) with 26% spaced closer than 500 nm. Analysis of the proximity of NR1 to contiguous Cx36 pairs revealed a significant fraction of NR1 closer than 150 nm from Cx36 in quadruple assemblies. Data in D-F were obtained from 131,076 $\mu m^3$ of IO neuropil in 15 tissue volumes.
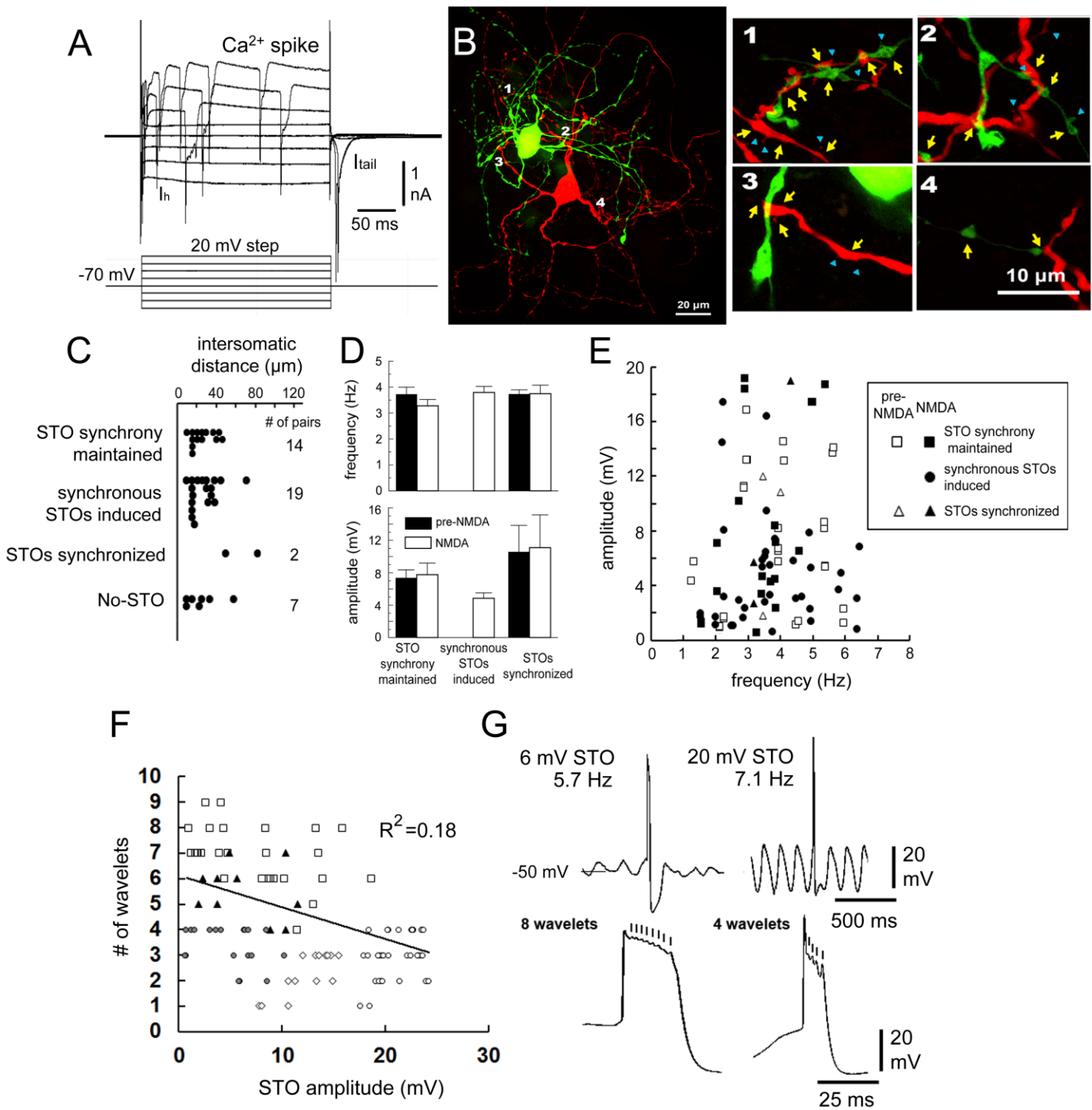
**Figure S2. Electrophysiological and anatomical identification of IO neurons and STO characteristics of coupled IO neurons, related to Figure 3.**

(A) Voltage steps originating from -70 mV were used to identify the membrane currents characteristic of IO neurons. Those included the presence of $I_h$ to negative voltage steps, a tail

current ($I_{tail}$) upon step from negative holding potential to -70 mV (composed of T-type calcium channel current and $I_h$ current during its inactivation; see Welsh et al., 2011), and broad $Ca^{2+}$ spikes triggered by positive voltage steps. Neurons were only included in the study if they showed those defining characteristics of IO neurons, which distinguished them from other neurons in the ventral brainstem. The recording also shows prominent fast $Na^+$ spikes in escape from voltage clamp, indicating fully intact membrane properties. (B) Characteristic dendritic anatomy of neighboring IO neurons labeled with Neurobiotin (red) and Neurobiotin-488 (green) show overlapping dendritic arbors and the presence of dendritic varicosities at the sites of dendritic overlap (yellow arrows in 1-4). Spines are indicated by blue arrowheads. (C) Scatterplot of intersomatic distances between 42 IO neuron pairs showing the 4 types of STO behavior described in the text. (D) Mean (± 1 SEM) STO frequency and STO amplitude before and during 50 μM NMDA for 3 groups of IO neuron pairs shown in (C). (E) Scatterplot of STO frequency vs. STO amplitude for all neurons in the 3 groups showing STOs before (open symbols) and during (filled symbols) NMDA. (F) Negative correlation between STO amplitude and the number of wavelets riding on the afterdepolarization (ADP) of entrained action potentials for individual spikes of 6 IO neurons. Values from individual spikes are plotted and each neuron is represented by a unique symbol. (G) Example of 2 neurons showing STO-entrained spikes. The neuron with the larger STO induced by NMDAR activation shows half as many wavelets riding on the ADP. Thus, the enhancement of STO amplitude by NMDAR activation can be associated with fewer wavelets consistent with a computational model in which the strengthening of electrical coupling is reflected in enhanced STO amplitude, a reduction in current across the GJ, and a negative influence on dendrosomatic coupling (De Gruijl et al., 2012).
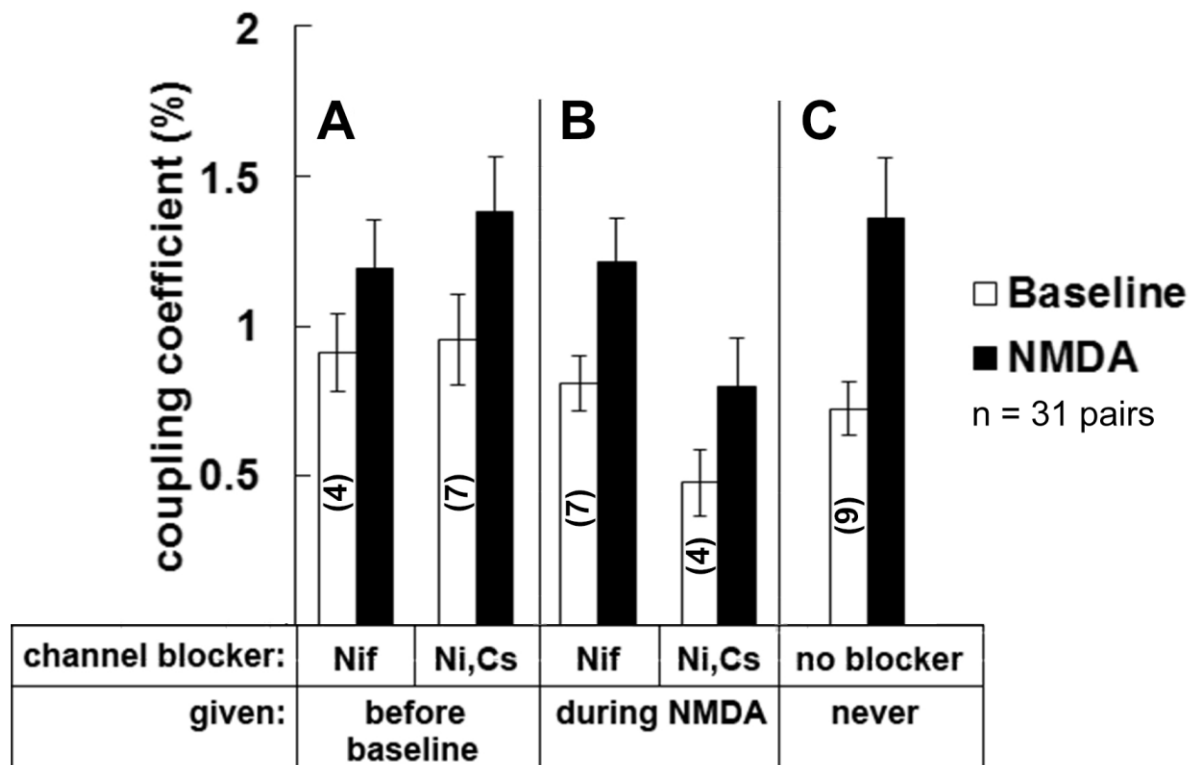
| channel blocker: | Nif | Ni,Cs | Nif | Ni,Cs | no blocker |
|---|---|---|---|---|---|
| given: | before baseline | | during NMDA | | never |

**Figure S3. Nifedipine and Ni/Cs do not affect baseline CC or its strengthening by NMDAR activation, related to Figure 4.**

Mean CC values (± 1 SEM) before and during NMDA for 2 groups of paired recordings in which nifedipine (Nif) or Ni/Cs (Ni,CS) were administered to block STOs (A and B) as compared to a third group of paired recordings that either never showed STOs or only very intermittently, and so were not administered nifedipine or Ni/Cs (C, No-STO group). In (A) nifedipine or Ni/Cs was administered prior to CC testing because both simultaneously-recorded cells showed STOs prior to NMDA (n=11 pairs). Nifedipine or Ni/Cs blocked STOs and subsequent administration of NMDA depolarized the neurons but did not induce STOs. In (B), nifedipine or Ni/Cs was not administered before NMDA was applied because they had a stable membrane potential that allowed baseline CC to be measured (n=11 pairs). For those pairs, NMDA induced STOs that were subsequently blocked by nifedipine or Ni/Cs to allow CC to be measured during NMDA. In (C), neither nifedipine nor Ni/Cs was delivered because

membrane potential was stable both before and during NMDA and CCs could be measured without the confound of STOs (n=9 pairs).

Repeated measures ANOVA of the CC values from all 3 groups detected a significant main effect of NMDA to increase CC [$F_{(1,59)}=25.7$, $p < 0.0001$] but did not detect a significant main effect of group [$F_{(2,59)}=1.7$, $p = 0.2$]. Repeated measures ANOVA of CC values from groups A and B also revealed a significant effect of NMDA to increase CC [$F_{(1,40)}=8.7$, $p < 0.01$] but did not detect significant main effects of blocker [$F_{(1,40)}=1.5$; $p = 0.23$], group [$F_{(1,40)}=2.3$, $p = 0.1$], or interaction of group x blocker x NMDA [$F_{(1,40)}=0.2$, $p = 0.7$]. The analyses indicated that treatment with nifedipine or Ni/Cs to block STOs did not affect the baseline CC or the ability of NMDA to enhance CC.
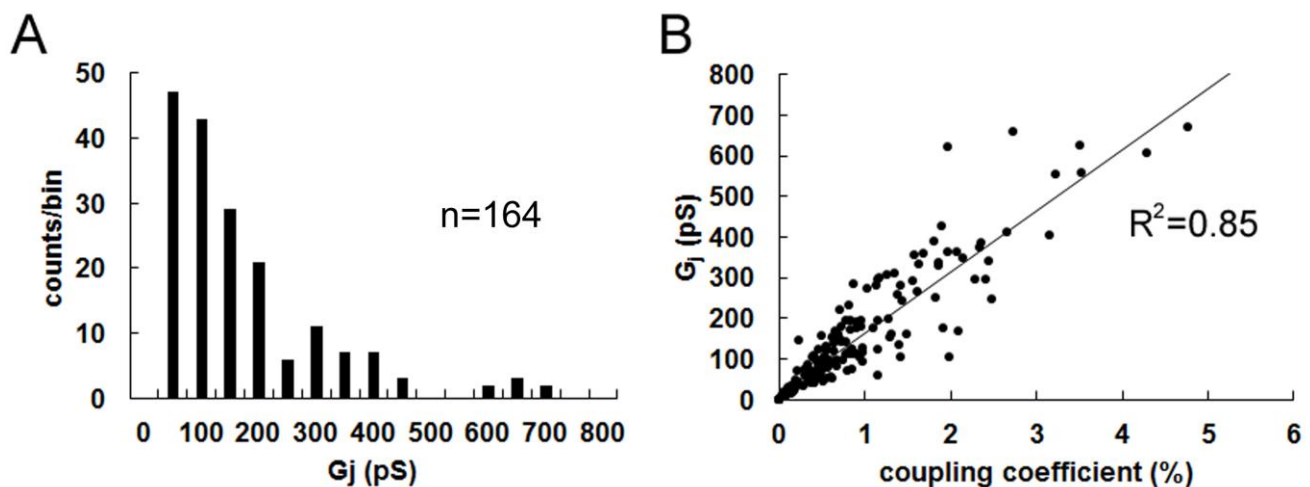


**Figure S4. Summary statistics of baseline $G_j$ in electrically-coupled IO neurons, related to Figure 5.**

(A) The distribution of $G_j$ for 164 directions of current injection (82 pairs) ranged from 50 to 750 pS, with a mode centered between 50 and 100 pS. The majority of $G_j$ measurements (75%) was less than or equal to 200 pS. (B) Calculated $G_j$ showed strong correlation to calculated CCs ($R^2 = 0.85$).

| Synaptic stimulation experiment | Figure | Baseline $G_{in}$ (nS) | During stimulation $G_{in}$ (nS) | Post-stimulation $G_{in}$ (nS) |
|---|---|---|---|---|
| **Normal ACSF (Ni/Cs to block STOs)** | | | | |
| 50 Hz burst, no blockers | 7B | 10.51 ± 0.67 | not measured | 10.37 ± 0.72 |
| PPS, no blockers | 7C black trace | 12.44 ± 0.55 | not measured | 12.90 ± 0.46 |
| PPS, MK-801 | 7C red trace | 9.70 ± 0.52 | not measured | 9.74 ± 0.68 |
| **$Mg^{2+}$-Free ACSF, bicuculline, ketanserin (Ni/Cs to block STOs)** | | | | |
| 9 Hz train | 7D | 14.06 ± 1.20 | 13.81 ± 0.98 | 12.43 ± 0.85 |
| 9 Hz train + CNQX | 7E black trace | 12.35 ± 1.28 | 13.43 ± 1.13 | 13.40 ± 1.16 |
| 9 Hz train + CNQX + TBOA | 7E red trace | 15.90 ± 1.59 | 15.15 ± 1.36 | 13.82 ± 1.45 |

**Table S1. Values of $G_{in}$ for all of the experimental groups in the synaptic stimulation experiments, related to Figure 7.** The table shows that there was no significant change in $G_{in}$ in comparing the epochs before, during, and after synaptic stimulation in any of the experiments (all $p > 0.05$ by t-test). Thus, the changes in CCs observed after PPS and 9 Hz stimulation and under various conditions were not attributable to a change in the leakiness of the non-junctional membrane.
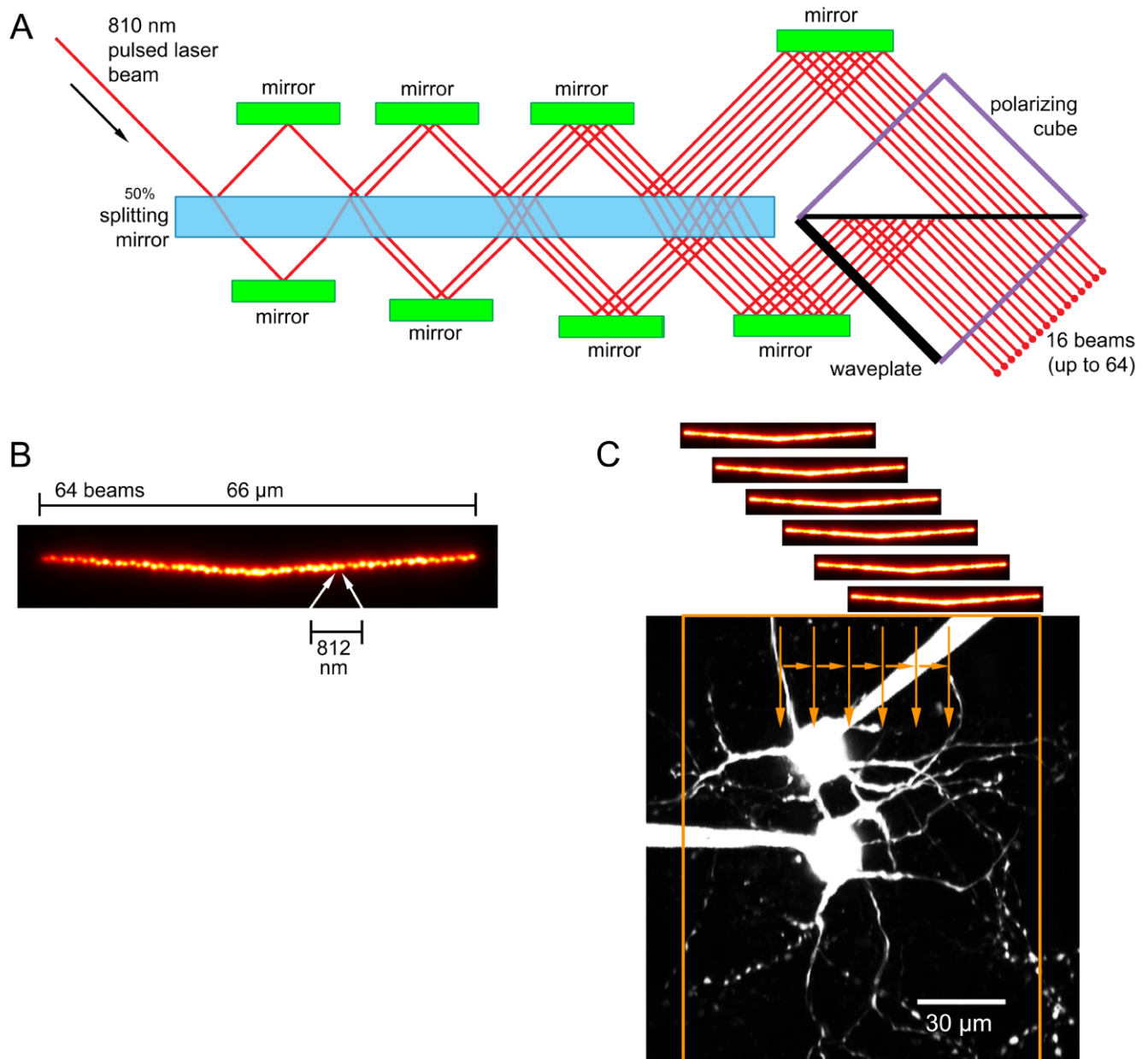
**SUPPLEMENTAL EXPERIMENTAL PROCEDURES**



**Figure S5. Rapid, full field-of-view (FOV) multibeam 2-p imaging (MMM imaging), related to Figure 8.**

Imaging the $Ca^{2+}$ dynamics from multiple DVs distributed throughout the interwoven dendritic arbors of two electrically-coupled IO neurons within thick tissue sections required a form of 2-p microscopy that allowed rapid, full FOV imaging. A common method for rapid 2-p microscopy

increases imaging rate by limiting the scanning of a single laser beam to a region of interest (ROI) that is a line (i.e. "line-scanning") or a small box ("box-scanning") that can be placed over multiple cellular structures organized in series or in a cluster. Fluorescence emission is captured with a photomultiplier tube that can image the ROI faster than 100 Hz during 64 pixel line-scanning or 8 Hz when a 64 x 64 pixel box is scanned (e.g. Sullivan et al., 2007). However, a challenge for the imaging of multiple DVs of electrically-coupled neurons is that they are small (~3 µm) and are randomly distributed over a large area, requiring full FOV imaging with higher frame rate and pixel resolution than can be achieved with line- or box-scanning.

An alternative is spatial-light modulator (SLM) 2-p microscopy (Nikolenko et al., 2008) that uses diffractive optics to split a 2-p laser beam into 50 to 100 beamlets each of which can be held fixed within as many ROIs, such as a cell bodies or dendritic spines, inside a large FOV. The use of stationary beamlets removes the time needed for scanning the beams over the FOV and can achieve acquisition rates for $Ca^{2+}$ imaging between 15 and 60 Hz by capturing fluorescence signals with a CCD camera (Nikolenko et al., 2008). One limitation of SLM microscopy for our experiments was that the beam-steering needed to prepare the experiment takes time and, therefore, is impractical when dual whole-cell recordings are established. A second limitation for our experiments was that SLM microscopy restricts signal acquisition to predetermined ROIs and leaves potentially important signals within different parts of the dendritic arbors uncaptured.

We chose a different 2-p imaging approach that combines the advantage of beam splitting with the advantage of scanning in order to achieve full FOV 2-p imaging at 40 Hz. This type of imaging, called multibeam multiphoton microscopy (MMM), is performed with a

scanhead (TriMScope, Lavision Biotec, Bielefeld Germany) that contains a mirror/splitter device shown in (A) based after Nielsen et al. (2001). A 2-p laser beam (red; 2.7 W at 810 nm, Spectra Physics MaiTai DeepSee HP) is attenuated to 32% then directed into a 50% splitting mirror (blue). A series of 6 pairs of laterally-positioned mirrors (green, only 4 pairs shown for simplicity) reflects the beamlets back into the splitting mirror until 32 beamlets are formed on each side of the mirror. One set of 32 beamlets is passed through a waveplate (thick black line) to change its polarity before the two sets are passed into a polarizing cube (purple) that aligns them with one another. The 64 beamlets, each ~11 mW, exit the polarizing cube as a line and are passed through an IR-corrected 20x microscope objective (Olympus XLUMPFL, 0.95 na) to excite a 66 µm length of tissue (B). The beam line is then scanned over the tissue in repeated vertical sweeps using 10 µm lateral translations between sweeps (C). This allows the full 130 x 130 µm FOV to be excited at 200 Hz. A high (> 62%) quantum efficiency CCD camera (1376 x 1040 pixels, Imager QE, LaVision Biotec) captures the emission fluorescence at 40 Hz, thereby integrating the emission of 5 full FOV scans in each 25 ms CCD frame capture to increase signal to noise.

**SUPPLEMENTAL REFERENCES**

Welsh, J. P., Han, V. Z, Rossi, D. J., Mohr, C., Odagiri, M., Daunais, J. B., and Grant, K.A. (2011). Bidirectional plasticity in the primate inferior olive induced by chronic ethanol intoxication and sustained abstinence. Proc. Natl. Acad. Sci. USA *108,* 10314-10319.

Nielsen, T., Fricke, M., Hellweg, D., and Andresen, P. (2001). High efficiency beam splitter for multifocal multiphoton microscopy. J. Microsc. *201,* 368-376.

Nikolenko, V., Watson, B. O., Araya, R., Woodruff, A., Peterka, D. S., and Yuste, R. (2008). SLM Microscopy: Scanless two-photon imaging and photostimulation with spatial light modulators. Front. Neural Circ. *2,* 5.

Sullivan, M. R., Nimmerjahn, A., Sarkisov, D. V., Helmchen, F., and Wang, S. S. (2005). In vivo calcium imaging of circuit activity in cerebellar cortex. J. Neurophysiol. *94,* 1636-1644.